Dalton Transactions

Accepted Manuscript

ROYAL SOCIETY OF CHEMISTRY

www.rsc.org/dalton

Cite this: DOI: 10.1039/c0xx00000x

www.rsc.org/xxxxxx

ARTICLE TYPE

In situ controlled sputtering deposition of gold nanoparticles on MnO_2 nanorods as surface-enhanced Raman scattering substrates for molecular detection

Tao Jiang,*[a] Li Zhang,[a] Han Jin,[b] Xiaolong Wang,[a] and Jun Zhou*[a]

Received (in XXX, XXX) Xth XXXXXXXXX 201X, Accepted Xth XXXXXXXXX 201X
DOI: 10.1039/b000000x

Single-crystal tetragonal α-MnO_2 nanorods attached with different amount of gold nanoparticles (NPs) were successfully prepared by a facile sputtering deposition technique. Initially, the morphology and crystal structure of the bare α-MnO_2 nanorods synthesized via hydrothermal approach were investigated. Then, the amount of gold NPs at different sputtering time was analyzed. It was confirmed that the amount of the decorated gold NPs increased with the lengthening of the sputtering time until completely wrapped up the α-MnO_2 nanorods. The theoretical calculation results indicated the advantage of the composite structure by showing the enhanced electromagnetic fields around both the bare α-MnO_2 nanorods and the gold NPs decorated ones. The surface-enhanced Raman scattering (SERS) efficiency of these nanocomposites was evaluated by using methylene blue and 4-mercaptobenzoic acid as Raman probe molecules. It was found that the SERS intensity of the substrates strongly depended on the aggregation degree of the gold NPs. Uniform SERS signals throughout the whole surfaces of these samples were obtained. Moreover, a typical chemical toxin namely methyl parathion was effectively detected over a broad concentration range from 1×10^{-3} to 100 ppm by using the gold NPs decorated α-MnO_2 nanorods, suggesting this hybrid structure is highly valuable for further applications on rapid detection of organic environment pollutants.

Introduction

Surface-enhanced Raman scattering (SERS), which opened an exciting research area for single molecule microscopy, has been extensively applied in chemical and biological sensors due to its selectivity, supersensitivity, rapid response, and in situ detection.[1-5] However, one of the most crucial challenges in the practical application of SERS is the Raman signal reproducibility, which is closely related to the homogeneity of the substrate.[6-8] On the other hand, intense SERS signals due to enhanced electromagnetic fields are often found around the aggregations of the metal nanoparticles (NPs) or their sharp corners. In spite of the simple realization of the colloidal metal aggregation, their uncontrolled aggregation degree usually yields the fluctuation of the SERS intensity.[9-13] Accordingly, to fabricate a substrate with both homogenous surface and high density of active spots is one of the key steps to overcome these problems.

At the early research stage of SERS, a great deal of attentions have been paid to the Group 11 metals (gold, silver, and copper) for their unique surface plasmon resonance (SPR) properties, which are extremely beneficial to the local electromagnetic field enhancement. Recently, SERS-active substrates have been expanded to non-Group 11 materials including metal oxides, silver halides, transition metals, and semiconductors with the mushroom development of nanotechnology.[12] The primary cause for these Raman enhancement phenomenons is attributed to the charge transfer mechanism. Particularly various gold or silver decorated TiO_2 hybrid nanostructures have been demonstrated as excellent SERS substrates.[14-16] It is important to note that their improved SERS activity stems from both the electromagnetic enhancement of the noble metal NPs and the chemical enhancement of the TiO_2. Therefore, it is reasonable to expect that other semiconductors with special structures may also be suitable to act as the stable, reproducible, and robust SERS substrate. One-dimensional manganese dioxides such as nanowires, nanorods, and nanotubes, which exhibit distinctive physical and chemical properties, have been successfully prepared and exploited in catalysis, ion exchange, biosensor, and energy storage.[17-20] Among them, α-MnO_2 nanorods can provide not only smooth surfaces for the homogeneous gold aggregation but also sharp edges to form hot spots. Reliable and stable SERS signals can be expected after the arrangements of gold NPs on the nanorods owing to the generation of homogeneous multiple hot spots and the propagation of SPRs. Meanwhile, the high surface to volume ratio of the nanorods allows the presentation of sufficient surface ligands to generate further stronger and distinctive signals.

So far, many techniques have been developed on the basis of combining metal NPs and the unique nanostructures, such as impregnation reduction, ultrasonic assistance reduction,

electrochemical deposition, and sputtering deposition.[21-23] Among them, sputtering deposition technique is more attractive due to its relatively simple equipments and controllable sputtering amount of noble metal NPs on solid surfaces.[21,24] When one-dimensional nanomaterials with flat surfaces were used as the SERS substrates, massive homogeneous noble metal NPs can form gradually with the increase of the sputtering time. Moreover, it is regarded as an extremely clean process, since metal NPs can be synthesized with neither chemical reactions nor additional capping and stabilizing agents. Consequently, the following SERS applications would not be impaired with the blocking effect of these agents on the target molecules being avoided.

In this research, a simple method was demonstrated for practical SERS applications by combining α-MnO_2 nanorods with gold NPs. The single-crystal α-MnO_2 nanorods with sharp ends were prepared by hydrothermal technique. By simply extending the deposition time, the α-MnO_2 nanorods were gradually wrapped up by the gold NPs. After calculating the electromagnetic field distribution around the bare α-MnO_2 nanorods and the gold NPs decorated ones by three-dimensional finite element method (FEM), it was found that not only the chemical enhancement but also the electromagnetic enhancement existed between the α-MnO_2 nanorods and probe molecules. As a result, intense SERS signals of methylene blue (MB) and 4-mercaptobenzoic acid (4MBA) were obtained in the gold NPs decorated α-MnO_2 nanorods. Furthermore, a typical chemical toxin namely methyl parathion (MP) was effectively detected over a broad concentration range from 1×10^{-3} to 100 ppm by using the hybrid structure.

Experimental

Preparation of samples

$KMnO_4$, HCl, and MP were purchased from Sigma-Aldrich. MB and 4MBA were obtained from J&K scientific Ltd. Milli-Q water (18.2 MΩ cm) was used throughout the whole experiment.

Single crystal α-MnO_2 nanorods were prepared via a facile hydrothermal method.[25] In detail, 5 mmol $KMnO_4$ and 20 mmol concentrated HCl were added to deionized water to form a total volume of 90 mL. Then, the above precursor solution was transferred to a 100 ml autoclave, sealed and maintained at 140 °C for 12 h. After the autoclave was cooled to room temperature naturally, the resulting precipitates were separated by centrifugation and washed with deionized water for characterization. During the hydrothermal reaction process, MnO_2 nanorods in situ grew on the silicon wafer, which was firstly placed in the autoclave. Then, the deposition of the gold NPs on the MnO_2 nanorods was performed in a small sputter coater (JS-1600) with a current of 30 mA under argon pressure of 5 Pa. Six as-prepared MnO_2 nanorods coated silicon wafers were sequently put on a horizontally settled stainless plate at a distance of 20 mm from the gold foil target (99.99% in purity). The sputtering time was set as 5, 10, 15, 20, 25, and 30 min and the resulting samples were defined as MnO_2@Au (1), MnO_2@Au (2), MnO_2@Au (3), MnO_2@Au (4), MnO_2@Au (5), and MnO_2@Au (6), respectively.

MB or 4MBA-labelled hybrid structures were prepared as follow: the α-MnO_2 nanorods decorated with different amount of gold NPs were immersed in MB or 4MBA (1 mM) ethanol solutions for 5 h, respectively. These substrates were then washed with ethanol and deionized water to successively remove the excess Raman report molecules. The overall procedure for the fabrication of the hybrid structure is illustrated in Scheme 1.

Instruments and measurement

The sizes and morphologies of the products were observed by a SU-70 FESEM and a TECNAI G2 F20 TEM. The phase structures of the products were identified by XRD using a Model Rigaku Ru-200b powder diffractometer with nickel-filtered Cu-Kα radiation (λ = 1.5406 Å). The operation voltage and current were 50 kV and 200 mA, respectively. The 2θ angle ranged from 10° to 70°. The SERS properties of the samples were examined by a miniature Raman spectrometer (BWS415, B&W Tek Inc.) using a 785-nm semiconductor laser as the excitation source. The specifications of the Raman spectrometer were set as follow: the laser power at the sample position was 49.55 mW and the accumulation time was 10 s; The scattered radiation was collected by a 40× objective lens with numerical aperture (NA) as 0.65 and dispersed by the grating of 1200 lines/mm, and then passed through a slit with 20 μm width to the charge-coupled device (CCD) (2048×2048 pixels) detector. All the analysis was performed at room temperature.

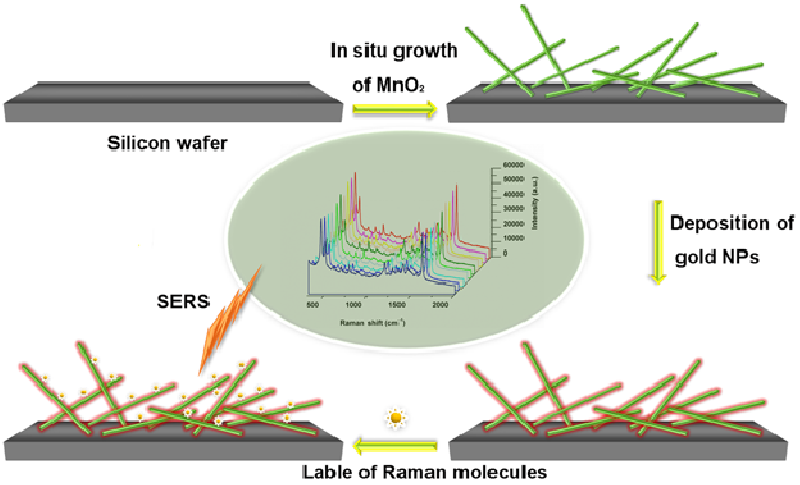

Scheme 1 Fabrication of gold NPs decorated α-MnO_2 nanorods on silicon wafer.

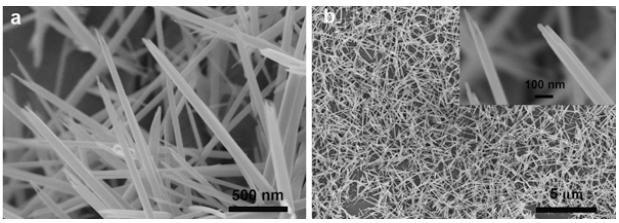

Fig. 1 (a), (b) SEM images of the α-MnO_2 nanorods, and the inset shows clearly the tiny tips of the samples.

Results and discussion

Figure 1 shows the SEM images of the as-prepared α-MnO_2 nanorods. All these nanorods possess flat and smooth surfaces as well as the tiny ends with diameters in the range of 30 to 50 nm, as presented in Fig. 1a. The larger scale SEM image in Fig. 1b shows that a large amount of α-MnO_2 nanorods has been successfully deposited on the silicon wafers. The tetragonal structure and rod shape of the samples were further confirmed by the TEM images in Figs. 2a and 2b. The tiny tops of the α-MnO_2 nanorods can also be discerned. The lattice fringes of the α-MnO_2 nanorods shown in the high-resolution TEM (HRTEM) images (Fig. 2) indicate the high crystallinity of these nanorods, and the measured lattice spacing is confirmed to be 0.50 nm, which is consistent with the d-spacing of the (200) plane of the tetragonal α-MnO_2 crystal (Fig 2c). The SAED pattern in Fig. 2d shows spotty single crystalline diffraction array corresponding to the (400), (200), (330), (420), and (440) planes of the α-MnO_2 lattice. Figure 3 presents the typical XRD pattern of the α-MnO_2 nanorods. It was found that all the diffraction peaks can be indexed to pure tetragonal α-MnO_2 (JPCDS 44-0141) without any other impurities. These results clearly indicate that high quality single-crystalline α-MnO_2 nanorods have been successfully prepared.

The representative SEM images of MnO_2@Au nanostructures with different amount of gold NPs are shown in Figs. 4a-4j and Figs. S1a-S1b (ESI†). The MnO_2 nanorods on the silicon wafer were found to overlap and interweave with each other, forming the coating platform. Additionally, most of the gold NPs in these hybrid structures were distributed on the surfaces of the MnO_2 nanorods. The density of gold NPs gradually increased with the elongation of the deposition time. As illustrated in Figs. 4a and 4b, tiny gold NPs sparsely disperse along the wide surfaces of MnO_2 nanorods in the sample synthesized with the deposition time for only 5 min. When the deposition time extended to 10 and 15 min, more and more isolated gold NPs with near spherical morphologies appeared on the MnO_2 nanorods (Figs. 4c-4f).

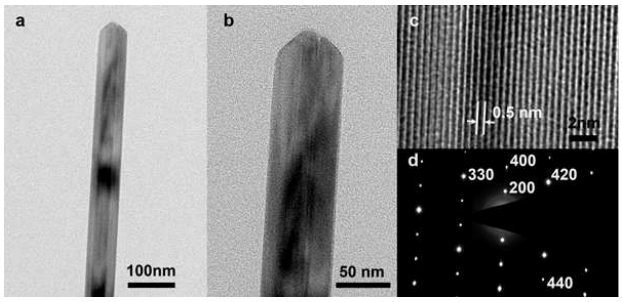

Fig. 2 (a), (b) TEM images, (c) HRTEM image, and (d) SAED pattern of the α-MnO_2 nanorods.

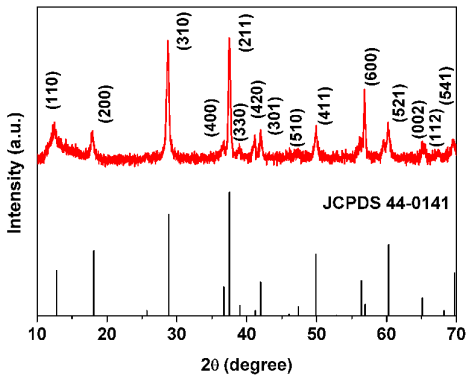

Fig. 3 XRD pattern of the α-MnO_2 nanorods.

After the deposition time further increased to 20 min, a great deal of gold NPs gradually connected with each other, leaving only a little bare surfaces of MnO_2 nanorods as presented in Figs. 4g and 4h. It is noteworthy that densely packed gold NPs were uniformly

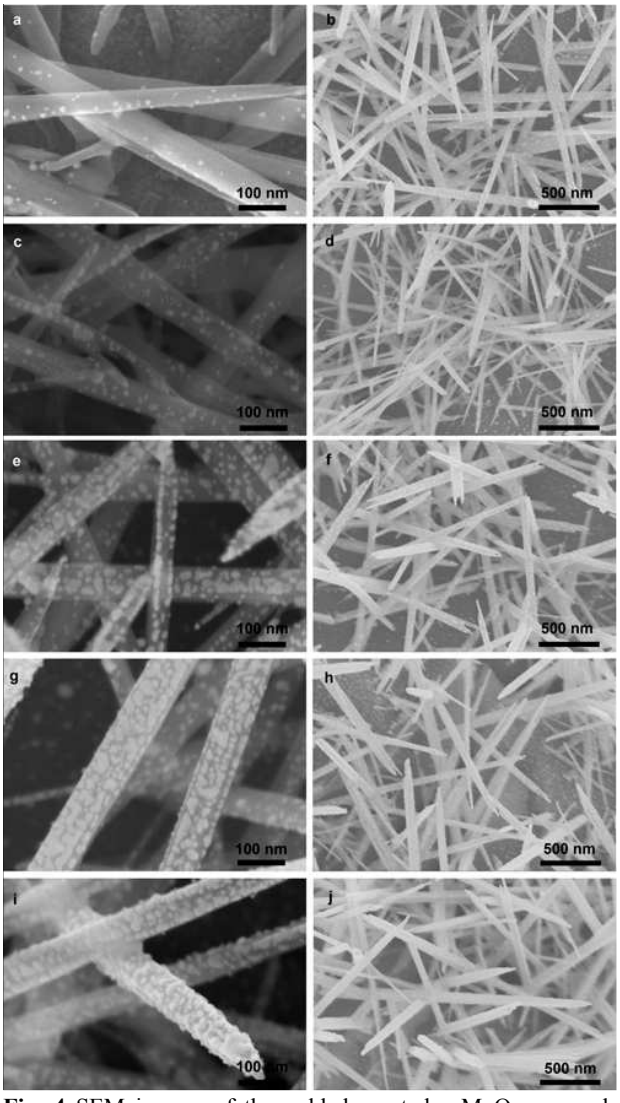

Fig. 4 SEM images of the gold decorated α-MnO_2 nanorods obtained after different deposition time: (a), (b) 5 min, (c), (d) 10 min, (e), (f) 15 min, (g), (h) 20 min, and (i), (j) 25 min.

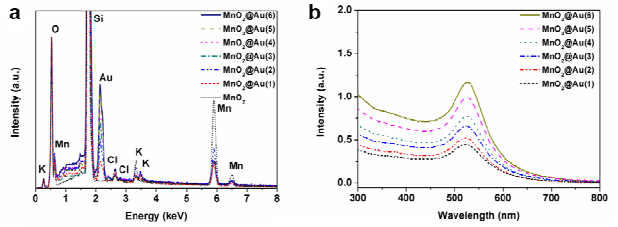

Fig. 5 (a) EDS and (b) absorption spectra of the gold decorated α-MnO_2 nanorods.

coated and completely covered the surfaces of MnO_2 nanorods when the deposition time reached 25 min as dedicated in Figs. 4i and 4j. Nearly all the MnO_2 nanorods exhibit hairy morphologies and the close distance of most adjacent gold NPs on their surfaces is about 10 to 20 nm. When the deposition time was finally expanded to 30 min. A great deal of neighboring gold NPs aggregate to form nearly continues gold nanoshells over the MnO_2 nanorods as shown in Figs. S1a and S1b (ESI†). It was found that the aggregation degrees of the gold NPs gradually became larger with extending the sputtering time, and the shapes of them became gradually irregular. The chemical compositions of one bare MnO_2 nanorods and six MnO_2@Au nanostructures were all analyzed by the energy dispersive spectrum (EDS) under FESEM as shown in Fig. 5a. The peaks of element oxygen and manganese from MnO_2 nanorods are the dominant and the peak of element kalium was also observed. The deposition of the gold NPs on the MnO_2 nanorods was verified by the noticeable peaks of element gold in the six hybrid samples. In order to further clearly discriminate the variation tendency of element gold, all the spectra were normalized at the peak of oxygen. It can be seen that the intensity of element gold gradually increases from sample MnO_2@Au (1) to MnO_2@Au (6), clearly indicates the successful covering of MnO_2 nanorods by gold NPs. As it is presented in Fig. 5b, the main absorption bands of these hybrid samples locate at around 532 nm and their peak intensities increase with the extension of the sputtering time. The irregular shapes of the gold NPs generated by the sputtering deposition

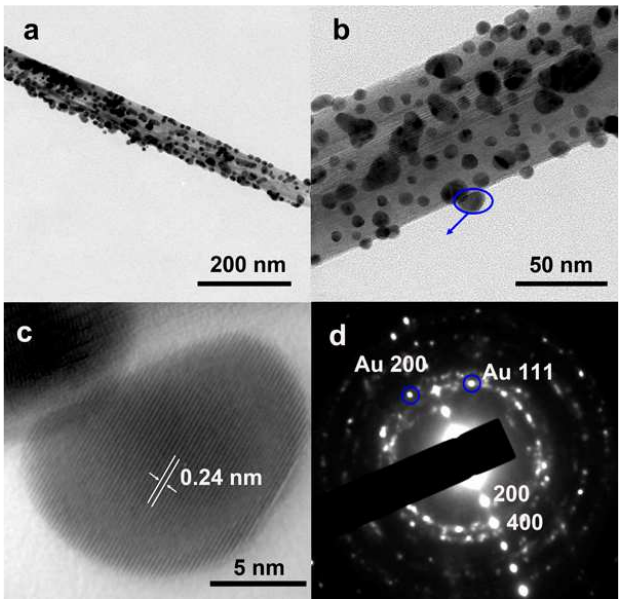

Fig. 6 (a), (b) TEM images, (c) HRTEM image, and (d) SAED pattern of the sample MnO_2@Au (5).

were further investigated by the TEM images, and these NPs adhere to the MnO_2 nanorods tightly as shown in Figs. 6a and 6b. Fig. 6c shows HRTEM image of a typical gold NP in the circle of Fig. 6b. The 0.24 nm lattice fringes could be indexed to the (111) spacing of gold, which extended across the entire irregular NP. The SAED pattern shows polycrystalline diffraction rings, which correspond to the (111) and (200) planes of the gold lattice besides the (200) and (400) planes of the MnO_2 lattice in Fig. 6d.

As it is well known, compared to the chemical enhancement, electromagnetic enhancement gives the major contribution to SERS. It is widely accepted that the collective oscillation of the surface electrons near the plasmon resonance induces such an enhanced electromagnetic field, which depends on the size, geometry, surface roughness, interparticle spacing, excitation wavelength, and dielectric environment. More intense electromagnetic field usually generated around the nanoscale aggregates, gaps, or junctions as a consequence of plasmon coupling. In this work, enhanced electromagnetic fields around both the bare MnO_2 nanorods and gold NPs decorated ones were firstly investigated by FEM based on the structures of the prepared samples as shown in Fig. 7. In these calculations, light sources with a central frequency equivalent to 785 nm were incident normally to the surfaces of the models in the x-axis and the polarization of the excitation was along the z-axis. Fig. 7a shows the E-field distribution of bare MnO_2 nanorods in the x-z plane. It can be clearly seen that an electromagnetic field existed around the MnO_2 nanorods with the diameters of 50 nm although the maximum electromagnetic field intensity is only 2.89. In previous literature, it was reported that the charge transfer between semiconductors such as TiO_2 and target molecules can induce the chemical enhancement of SERS signal.[15,16] Furthermore, it is proved in this work that enhancement electromagnetic field also exists on the MnO_2 nanostructures, indicating their potential advantage in SERS. This discovery may lead to further enthusiasms for non-Group 11 materials in the field of SERS. However, thorough and in-depth works are needed to be carried out. The incorporation of 10 nm gold nanoshell onto the MnO_2 nanorods induced significant changes to the electromagnetic field and the maximum intensity increased significantly to 26.3 as presented in Fig. 7b. As it is known that the enhancement factor of the electromagnetic field due to the excitation of SPR in the metallic nanostructures is the biquadratic of the simulated electromagnetic intensity.[26] Therefore, the largest enhancement factor of E-field intensity in this configuration is about 4.78×10^5. Besides, rough surfaces such as nanotips in particular can also induce hot spots, which are much

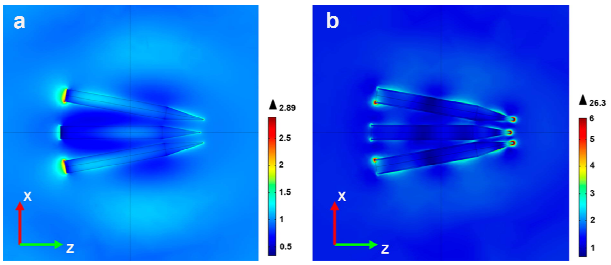

Fig. 7 FEM simulation of the E-field intensity distributions of (a) α-MnO_2 nanorods and (b) gold decorated α-MnO_2 nanorods with incident laser wavelength of 785 nm.

desired in SERS application. There are many distinctive tiny tops in the synthesized MnO_2 nanorods as shown in Figs. 1 and 4, which possesses superiorities to the TiO_2 nanorod, nanopore, and nanotube.[27] It is obvious that the maximum electric fields appear mostly around the tiny tips to form the so-called hot spots. The SERS efficiency of the hybrid nanostructure under the excitation of 532 nm has also been simulated by the FEM and the maximum electromagnetic field intensities increase obviously compared to those under the illumination of 785 nm as displayed in Fig. S2 (ESI†). Although the simulation model was not exactly the same with the actual hybrid nanostructure, a strongly amplified electromagnetic field can be induced by the SPR effect of the gold in the nanostructures, which can be well confirmed by the simulation.

The prepared samples have been theoretically proved to maintain enhanced electromagnetic field. To further experimentally evaluate the SERS activity of the prepared gold decorated α-MnO_2 nanorods, MB and 4MBA were selected as the target molecules, respectively. As a non-destructive spectroscopy analysis technique, the SERS is more suitable to detect the biological tissues by using the incident radiation in the "window of optical transparency", i.e. near infrared spectral region of 750-1000 nm. Therefore, a Raman spectrometer with excitation wavelength of 785 nm was chose in the following experiments. The Raman spectra of the samples depend on the amount of the decorated gold NPs are depicted in Fig. 8 and gradually noticeable Raman signals were obtained. As illustrated in Fig. 8a, the characteristic Raman peaks of MB can be obviously observed. The peak at 449 cm^{-1} occurs from the C–N–C deformation mode. The band at 1396 and 1436 cm^{-1} is assigned to the symmetric and asymmetric C–N stretches, respectively. The peak at about 1610 cm^{-1} results from the mode of the C–C ring stretch.[28] The characteristic Raman peaks of MB with a little low intensity can be obviously observed in the SERS spectrum of bare MnO_2 substrates, which is similar to that of the MnO_2@Au (1). The reason for this phenomenon is that the electromagnetic enhancement effect was not remarkable for the substrate of MnO_2 attached with a small amount of gold NPs. Most of the Raman report molecules could bond with the MnO_2 nanorods rather than gold NPs, which could cause the charge transfer effect between MnO_2 and report molecules. The mechanisms for the Raman spectrum enhancement were the chemical and electrical enhancement although the enhanced electromagnetic fields existed around the bare MnO_2 were a little weak as calculated by the FEM. These results were approved by the SERS spectra of the 4MBA labeled substrates of MnO_2 and MnO_2@Au (1), in which, the characteristic band intensities of 4MBA were almost the same as shown in Fig. 8b. In the Raman spectra of 4MBA, two dominant peaks at 1076 and 1586 cm^{-1} are assigned to the ring breathing modes. The band at 849 cm^{-1} is attributed to the COO^- bending mode (δ(COO^-)) and that at 1144 cm^{-1} is attributed to a mixed mode (13β(CCC) + ν(C–S) + ν(C–COOH)). Besides, the one at 1432 cm^{-1} is ascribed to the $\nu_s(COO^-)$ stretching mode.[29] Comparatively, the Raman peak intensities of both MB and 4MBA gradually increased from MnO_2@Au (2) to MnO_2@Au (5) substrate. With the increase of the coated gold NPs, the report molecules could mostly bond with the outside gold NPs rather than the MnO_2 nanorods. The electromagnetic enhancement progressively surpassed the chemical enhancement, which can be supported by the above simulation results that more intense electromagnetic field existed around the MnO_2 nanorods coated completely by gold NPs. Moreover, it is well known that the plasmon resonance properties of metal NPs are strongly dependent on their aggregation level. As the density of the gold NPs increases, the distance between these NPs decreases, the coupled plasmon resonance contributes to the enhancement of SERS signal. From the SEM and TEM images (Figs. 4 and 6), it has been seen that the diameters of the individual gold NPs in MnO_2@Au (5) and most of their interparticle gaps are about 10 to 20 nm. So both the small size and gap might generate a large amount of surface hot spots in the sample.[30] However, the hot spots in the small gaps between neighboring gold NPs decrease and even tend to disappear in the sample MnO_2@Au (6) due to the formation of nearly continues gold nanoshells, leading to the deteriorate of their SERS activates compared to those of the MnO_2@Au (5) (Figs. S1c and S1d, ESI†). Therefore, the optimal sputtering time is 25 min.

As it is reported, the increase of the noble metal NP size usually induces red-shift of their SPR band.[31] Consequently, the SERS efficiency of the noble metal will be affected significantly due to the SPR band moving away or close to the excitation wavelength. It can be seen that red-shift of the main absorption peak of the gold NPs decorated MnO_2 nanorods is not so obvious with the increase of the sputtering time (Fig. 5b). So, it is inferred that the increase of the SERS signals were mainly due to the formation of more and more hot spots on the aggregations of the gold NPs.

The peak at 449 and 1624 cm^{-1} (the two strong bands in the spectra) were employed to estimate the enhancement factors (EFs) through the following equation:

$$EF = (I_{SERS} \times N_{bulk})/(I_{bulk} \times N_{SERS})$$

Where I_{SERS} and I_{bulk} are the intensities of the same Raman band for the SERS and bulk Raman spectra. N_{bulk} is the number of molecules on a bulk sample, and N_{SERS} represents the number of molecules on a SERS sample. It should be pointed out that it was very difficult to estimate the exact number of molecules

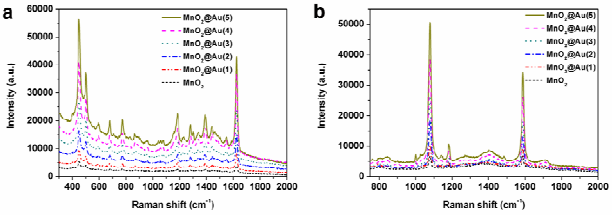

Fig. 8 Raman spectra of (a) MB and (b) 4MBA on the α-MnO_2 nanorods attached with different amount of gold NPs.

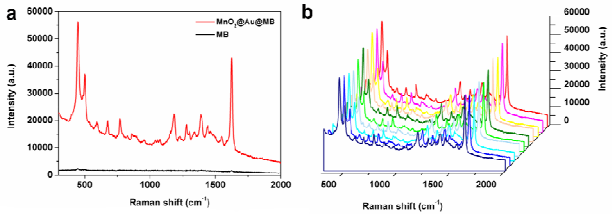

Fig. 9 (a) SERS spectrum of MB on the MnO_2@Au (5) and the normal Raman spectrum of MB in ethanol solution and (b) Raman spectra of MB collected from twenty measured sites on the MnO_2@Au (5).

immobilized on the MnO_2@Au (5) nanostructures. Thus, the intensity of the peaks at 449 and 1624 cm^{-1} were only used to roughly calculate the EF values because of their strong intensities in the spectra. N_{bulk} was determined to be 1.00×10^{12} on the basis of the Raman spectrum of a 1 mM MB solution and the focal volume of our Raman system as 1.66 μm^3. N_{SERS} was calculated to be 1.25×10^7 according to the assumption that a monolayer of molecules was formed on the surfaces of MnO_2@Au (5) substrates. The intensities I_{SERS} and I_{bulk} were determined to be 3.04×10^7 and 1.51×10^6 by the areas of the 449 cm^{-1} bands in the SERS spectra of MB labeled MnO_2@Au (5) as well as the normal Raman spectra of MB recorded from the ethanol solution under the same condition as shown in Fig. 9a. As a result, the EF value of this MnO_2@Au (5) substrate was calculated to be 1.61×10^6, which is higher than the simulation results. The reason can be explained as follow. In the simulation model, only three MnO_2 nanorods decorated with continuous gold shell are considered. By contrast, large amount of real hybrid nanostructures can provide plenty of nanotips and aggregations, SPRs spread and couple around these places to form the larger electromagnetic field. Simultaneously, both surface roughness and chemical enhancements, which are not accounted for in the simulations, are expected to increase the total SERS enhancement.[32]

The SERS reproducibility of the silver NPs, a vital factor for their applications, was also evaluated based on MB. Fig. 9b represents the measured SERS signals from different probe sites, which were randomly selected on the MnO_2@Au (5) nanostructures modified with MB molecules. The intensities of the peaks at 449 and 1624 cm^{-1} are chosen as parameters to character the reproducibility of the SERS enhancement as provided in Fig. 9b. It can be found that the intensities of SERS signals on different sites of the samples are nearly consistent. The relative standard deviations of the 449 and 1624 cm^{-1} peak intensities were calculated to be 7.63% and 9.78%, respectively. The strongly enhanced intensity as above 10^6 and the small dispersion of signals within 10% imply the MnO_2@Au (5) nanostructures as effective SERS substrates for many potential applications.

One of the applications is the continuous monitoring of toxin molecules. In this experiment, an important chemical and biological dangerous agent MP was detected by using the MnO_2@Au (5) substrate. In a typical experiment, appropriate amounts of toxin solutions (1×10^{-3} to 100 ppm) were dropped onto MnO_2@Au (5) substrates and aged for 5 h under room condition. Figure 10a illustrates the representative Raman spectra of the toxin agent. Strong Raman signals with high signal-to-noise ratios were obtained for the whole concentration range. The most prominent peak of MP at 1345 cm^{-1} was selected to determine the dependency of Raman intensities on toxin concentration. The intensities of related band increased with the concentration of toxin molecule as presented in Fig. 10b. A relatively good linearity was detected over a wide range of concentrations. The plot for the concentration-dependent SERS intensity of the band at 1345 cm^{-1} obeys the linear equation: $Y = 6738.73 + 29372.02X$, $R^2 = 0.987$, where Y is the SERS intensity of the band at 1345 cm^{-1}, and X is the concentration of MP. The detection limit for MP was found to be about 1×10^{-3} ppm.

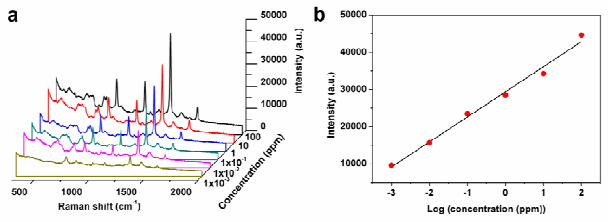

Fig. 10 (a) Detection of MP at different concentrations from 1×10^{-3} to 100 ppm based on SERS spectra and (b) the corresponding calibration curve.

Conclusions

In conclusion, a simple method was developed to detect chemical toxin using gold NPs attached α-MnO_2 nanorods as SERS substrate. The single-crystal α-MnO_2 nanorods with sharp ends were firstly prepared by hydrothermal technique. Then, α-MnO_2 nanorods attached with different amount of gold NPs were synthesized by a sputter deposition method. The enhanced electromagnetic field around the bare α-MnO_2 nanorods was certified by theoretical simulation results. As a result, intense and stable SERS signals of MB and 4MBA were obtained in the gold NPs decorated α-MnO_2 nanorods. The relative standard deviations of the 449 and 1624 cm^{-1} peak intensities of MB were only 7.63% and 9.78%. Furthermore, a typical chemical toxin MP was detected over a broad concentration range from 1×10^{-3} to 100 ppm with high signal to noise ratios, showing their potential practical applications.

Acknowledgments

This work was supported by the National Natural Science Foundation of China (NSFC) (Grant Nos. 11404177, 61275153, and 61320106014), the Natural Science Foundation of Zhejiang (Grant Nos. LY12A04002 and LQ14F040002), the Natural Science Foundation of Ningbo (Grant Nos. 2010D10018 and 2012A610107, and 2014A610120), the Foundation of Zhejiang Educational Commission (Grant Nos. Y201430403 and Y201430419), and K. C. Wong Magna Foundation of Ningbo University, China.

Notes and references

[a] *Department of Microelectronic Science and Engineering, Faculty of Science, Ningbo University, Ningbo 315211, P. R. China. Fax: 86-574-87600744; Tel: 86-574-87600794; E-mail: jiangtao@nbu.edu.cn zhoujun@nbu.edu.cn*

[b] *Gas Sensors & Sensing Technology Laboratory, Collage of Information Science and Engineering, Ningbo University, Ningbo 315211, P. R. China.*

† Electronic Supplementary Information (ESI) available: [details of any supplementary information available should be included here]. See DOI: 10.1039/b000000x/

1 J. M. Nam, C. S. Thaxton and C. A. Mirkin, Science, 2003, **301**, 1884–1886.
2 C. Y. Song, Z. Y. Wang, R. H. Zhang, J. Yang, X. B. Tan and Y. C. Cui, Biosen. Bioelectron., 2009, **25**, 826–831.
3 J. M. Su, G. F. Wang, Y. Li, R. Li, B. Y. Xu, Y. P. Wang and J. S. Zhang, Dalton Trans., 2014, **43**, 14720–14725.
4 T. Jiang, L. Zhang and J. Zhou, Analyst, 2014, **139**, 5893–5900.
5 Q. F. Fan, J. Cao, Y. Liu, B. Yao and Q. H. Mao, Appl. Opt., 2013, **25**, 6163–6169.
6 S H. Im, K. C. Bantz, N. C. Lindquist, C. L. Haynes and S. Oh, Nano Lett., 2010, **10**, 2231–2236.

7 T. Gao, Y. Q. Wang, K. Wang, X. L. Zhang, J. N. Dui, G. M. Li, S. Y. Lou and S. M. Zhou, Appl. Mater. Interfaces, 2013, **5**, 7308–7314.

8 X. F. Li, M. H. Cao, H. Zhang, L. Zhou, S. Cheng, J. L. Yao and L. J. Fan, J. Colloid Interface Sci., 2012, **382**, 28–35.

9 M. Suzuki, Y. Niidome, Y. Kuwahara, N. Terasaki, K. Inoue and S. Yamada, J. Phys. Chem. B, 2004, **108**, 11660–11665.

10 K. L. Wustholz, A. I. Henry, J. M. McMahon, R. G. Freeman, N. Valley, M. E. Piotti, M. J. Natan, G. C. Schatz and R. P. V. Duyne, J. Am. Chem. Soc., 2010, **132**, 10903–10910.

11 C H. Zhu, M. L. Du, M. L. Zou, C. S. Xu and Y. Q. Fu, Dalton Trans., 2012, 41, 10465–10471.

12 A. B. Zrimsek, A. I. Henry and R. P. V. Duyne, J. Phys. Chem. Lett., 2013, **4**, 3206–3210.

13 P. Delange, Y. L. Ho and J. J. Delaunay, Appl. Opt., 2013, **52**, 8809–8816.

14 X. T. Wang, W. S. Shi, G. W. She and L. X. Mu, Phys. Chem. Chem. Phys., 2012, **14**, 5891–5901.

15 X. X. Zou, R. Silva, X. X. Huang, J. F. A. Sharab and T. Asefa, Chem. Commun., 2013, **49**, 382–384.

16 K Y. B. Xie, Y. Y. Jin, Y. Z. Zhou and Y. Wang, Appl. Surf. Sci., 2014, **313**, 549–557.

17 X. Wang and Y. Li, Chem. Commun., 2002, **124**, 764–765.

18 J. B. Yang, X. D. Zhou, W. J. James, S. K. Malik and C. S. Wang, Appl. Phys. Lett., 2004, **85**, 3160.

19 H. Wang, Z. Lu, D. Qian, Y. Li and W. Zhang, Nanotechnology, 2007, **18**, 115616.

20 D. Zheng, S. Sun, W. Fan, H. Yu, C. Fan, G. Cao, Z. Yin and X. Song, J. Phys. Chem. B, 2005, **109**, 16439–16443.

21 T. Suzuki, K. Okazaki, S. Suzuki, T. Shibayama, S. Kuwabata and T. Torimoto, Chem. Mater., 2010, **22**, 5209–5215.

22 J. M. Moon and A. Wei, J. Phys. Chem. B, 2005, **109**, 23336–23341.

23 A. U. Zillohu, R. Abdelaziz, M. K. Hedayati, T. Emmler, S. Homaeigohar and M. Elbahri, J. Phys. Chem. C, 2012, **116**, 17204–17209.

24 Y. Hatakeyama, T. Morita, S. Takahashi, K. Onishi and K. Nishikawa, J. Phys. Chem. C, 2011, **115**, 3279–3285.

25 J. Luo, H. T. Zhu, H. M. Fan, J. K. Liang, H. L. Shi, G. H. Rao, J. B. Li, Z. M. Du and Z. X. Shen, J. Phys. Chem. C, 2008, **112**, 12594–12598.

26 K. Keipp, Y. Wang, H. Kneipp, L. T. Perelman, I. Itzkan, R. R. Dasari and M. S. Feld, Phys. Rev. Lett., 1997, **78**, 1667–1670.

27 J. P. Li, J. Zhou, T. Jiang, B. B. Wang, M. Gu, L. Petti, and P. Mormile, Phys. Chem. Chem. Phys., 2014, **16**, 25601–25608.

28 B. Paramanik and A. Patra, J. Mater. Chem. C, 2014, **2**, 3005–3012.

29 A. Michota and J. Bukowska, J. Raman Spectrosc., 2003, **34**, 21–25.

30 Q. T. Zhou, G. W. Meng, Q. Huang, C. H. Zhu, H. B. Tang, Y. W. Qian, B. Chen and B. S. Chen, Phys. Chem. Chem. Phys., 2014, **16**, 3686–3692.

31 T. X. Tan, C. G. Tian, Z. Y. Ren, J. Yang, Y. J. Chen, L. Sun, Z. T. Li, A. P. Wu, J. Yin and H. G. Fu, Phys. Chem. Chem. Phys., 2013, **15**, 21034–21042.

32 K. L. Wustholz, A. Henry, J. M. McMahon, R. G. Freeman, N. Valley, M. E. Piotti, M. J. Natan, G. C. Schatz and R. P. V. Duyne, J. Am. Chem. Soc., 2010, **132**, 10903–10910.

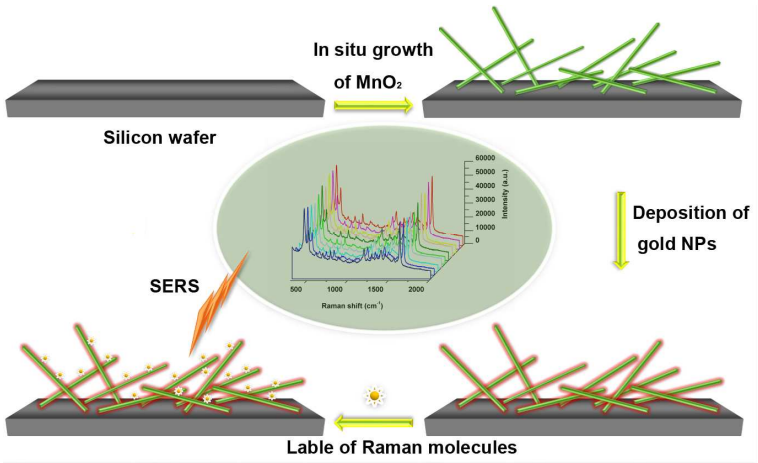

Single-crystal tetragonal α-MnO_2 nanorods attached with different amount of gold nanoparticles (NPs) were successfully prepared by a facile sputtering deposition technique. Initially, the morphology and crystal structure of the bare α-MnO_2 nanorods synthesized via hydrothermal approach were investigated. Then, the amount of gold NPs at different sputtering time was analyzed. It was confirmed that the amount of the decorated gold NPs increased with the lengthening of the sputtering time until completely wrapped up the α-MnO_2 nanorods. The theoretical calculation results indicated the advantage of the composite structure by showing the enhanced electromagnetic fields around both the bare α-MnO_2 nanorods and the gold NPs decorated ones. The surface-enhanced Raman scattering (SERS) efficiency of these nanocomposites was evaluated by using methylene blue and 4-mercaptobenzoic acid as Raman probe molecules. It was found that the SERS intensity of the substrates strongly depended on the aggregation degree of the gold NPs. Uniform SERS signals throughout the whole surfaces of these samples were obtained. Moreover, a typical chemical toxin namely methyl parathion was effectively detected over a broad concentration range from 1×10^{-3} to 100 ppm by using the gold NPs decorated α-MnO_2 nanorods, suggesting this hybrid structure is highly valuable for further applications on rapid detection of organic environment pollutants.